Numerical Inversion of Circular arc Radon Transform

Tabish A. Syed, Venkateswaran P. Krishnan, and Jayanthi Sivaswamy

Abstract—Circular arc Radon (CAR) transforms associate to a function, its integrals along arcs of circles. The inversion of such transforms is of natural interest in several imaging modalities such as thermoacoustic and photoacoustic tomography, ultrasound, and intravascular imaging. Unlike the full circle counterpart—the circular Radon transform—which has attracted significant attention in recent years, the CAR transforms are scarcely studied objects. In this paper, we present an efficient algorithm for the numerical inversion of the CAR transform with fixed angular span, for the cases in which the support of the function lies entirely inside or outside the acquisition circle. The numerical algorithm is noniterative and is very efficient as the entire scheme, once processed, can be stored and used repeatedly for reconstruction of images. A modified numerical inversion algorithm is also presented to reduce the artifacts in the reconstructed image which are induced due to the limited angular span.

Index Terms—Circular arc Radon transform, circular Radon transform, streak artifacts, trapezoidal product integration method, truncated singular value decomposition, volterra integral equations.

I. INTRODUCTION

CIRCULAR arc Radon (CAR) transforms involve the integrals of a function on a plane along a family of circular arcs. Our study of these transforms is motivated by its potential applications in imaging modalities such as thermoacoustic and photoacoustic tomography (TAT/PAT), ultrasound, radar and intravascular imaging.

In TAT/PAT the object of interest is irradiated by a short electromagnetic (EM) pulse. The irradiated tissue absorbs some of the EM energy, with the amount depending on tissue characteristics. Cancerous cells, for example, absorb more energy than the healthy cells due to high metabolic activity. It is diagnostically useful to know the EM absorption properties of tissues [1]–[5]. The absorption of EM energy causes an increase in the local temperature and makes the tissues expand and leads to a pressure distribution in the tissue, which is roughly proportional to the absorption function. The resultant pressure wave $p(t, x)$ propagates through the object and is measured by ultra-

sonic receivers/transducers located on an observation surface P surrounding the object. The goal of imaging is to use the measured data to reconstruct the initial pressure $p(0, x)$. Assuming that the background acoustic wave speed is a constant and that the transducers are omni-directional, the measured data can be modeled as a spherical Radon transform of the initial pressure distribution $p(0, x)$ with centers on the acquisition surface P [6]. Furthermore, assuming linear integrating detectors [7] or detectors focused to a plane [9], the 3-dimensional TAT/PAT problem can be recast as a slice-by-slice inversion problem for the 2-dimensional circular Radon transform.

However, in practical imaging systems, the aperture of detectors may be limited. Therefore, we consider a scenario where limited angular aperture detectors are used to collect data similar to [8], [10]. Assuming that tomographic data collection is restricted to a plane, the data measured by the limited angular aperture detectors can be modeled as a CAR transform with centers on the intersection of the plane with the acquisition surface P.

The transform involved in this setup associates for a given function, its integrals along circular arcs with *fixed angular span* instead of integrals along full circles. Additionally, in some imaging problems, full data in the radial direction may not be available, for instance, in the case of imaging the surrounding region of a bone. We consider these two imaging scenarios together and they serve as the main motivation for our study of CAR transforms in this paper. We recall that the case of partial data in the radial direction for circular and elliptical Radon transforms was considered in [11], [12]. Two related works where circular arc means transform have appeared are in SAR imaging [14] and Compton scattering tomography [15]. These use different setups: In [14], data is acquired along semicircular arcs of different radii with each semicircular arc being centred on a line segment, while, in [15] data is acquired along circular arcs with a chord of fixed length. These differ from the circular acquisition geometry we consider where data is acquired along arcs of different radii but with fixed angular span (see Fig. 1).

Our setup leads to a non-standard integral transform, described in Section II, which has not been considered previously. Specifically, in our situation, we have a Volterra integral equation of the first kind with a weakly singular kernel, in which both the upper and lower limits of the integral are functions. Integral equations of this kind, that is, ones with variable upper and lower limits, have been investigated in previous studies [16]–[20]. However, to the best of our knowledge, the integral equation that we encounter in this work does not seem to fit into these previously established results. In the current article, we present an efficient numerical inversion of the Volterra integral equation of the first kind appearing in the inversion of the CAR transform. Our work is based on the numerical algorithm for the inversion of a Volterra integral equation re-

T. A. Syed and J. Sivaswamy are with the International Institute of Information Technology, Hyderabad 500032, India (e-mail: syed.abbas@research.iiit.ac.in; jsivaswamy@iiit.ac.in).

V. P. Krishnan is with TIFR Centre for Applicable Mathematics, Bangalore 560065, India (e-mail: vkrishnan@math.tifrbng.res.in).

Fig. 1.   Measurement Setup.
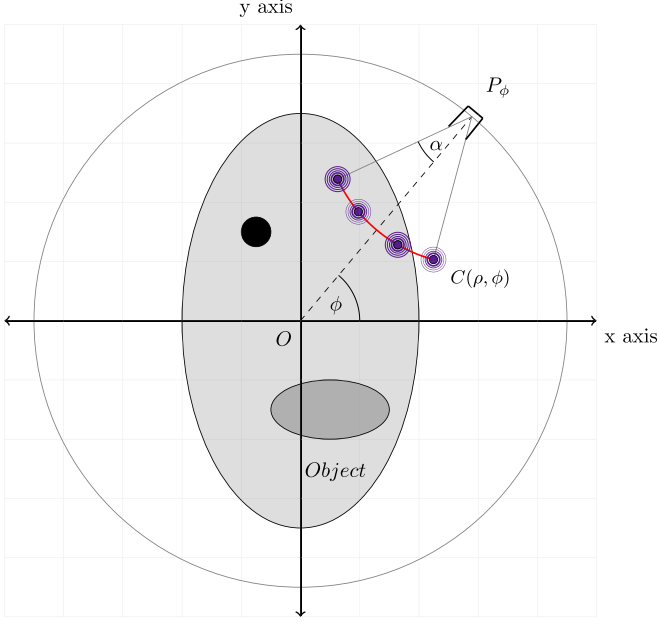

Fig. 2.   Setup for functions supported inside the acquisition circle.

cently published in [21] that used the trapezoidal product integration method [22], [23]. The inversion techniques of [21] have also been employed in the numerical inversion of a broken ray transform [24]. Unlike the situation in [21], the difficulty in our setup include the presence of edges of the circular arcs (see Fig. 1) and restricted visibility (in the sense of microlocal analysis [25], [26]) due to fixed angular span of the arcs. Due to these reasons the reconstruction algorithm introduces severe artifacts in the reconstructed image. Hence we propose an artifact reduction strategy in this paper. This paper is organized as follows. Section II gives the relevant nonstandard Volterra integral equations of the first kind involved in the study of CAR transform. Section III gives the numerical algorithm for inverting these Volterra integral equations of first kind. Section IV presents details of some experiments done in numerical reconstruction along with the results. V offers a solution to suppress artifacts arising in numerical inversion of the CAR transform. Finally, Section VI summarizes the paper.

II. CIRCULAR ARC RADON TRANSFORM

A. Function Supported Inside Acquisition Circle

Let (r, θ) denote the standard polar coordinates on the plane and let $f(r, \theta)$ be a continuous compactly supported function on $[0, \infty) \times [0, 2\pi)$ such that $f(r, 0) = f(r, 2\pi)$ for all $r \geq 0$. Let $P(0, R)$ denote a circle (acquisition circle) of radius R centered at the origin $O = (0, 0)$ and parametrized as follows:

$$P(0, R) = \{(R\cos\phi, R\sin\phi) : \phi \in [0, 2\pi)\}.$$

We consider the CAR transform $(\mathcal{R}_\alpha f)(\rho, \phi)$ of function $f(r, \theta)$ along circular arcs of fixed angular span α. The details of the setup are illustrated in Fig. 2.
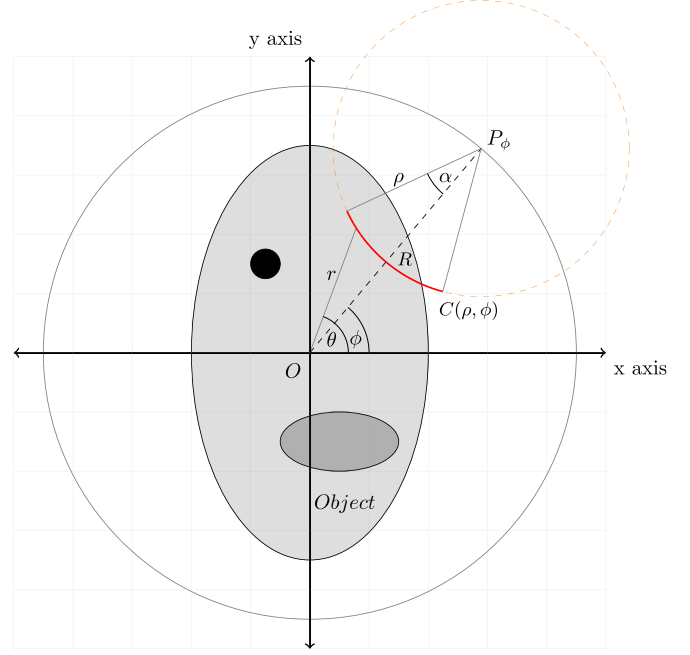
Let $C(\rho, \phi)$ be the circle of radius ρ centered at $P_\phi = (R\cos\phi, R\sin\phi)$. That is,

$$C(\rho, \phi) = \{(r, \theta) \in [0, \infty) \times [0, 2\pi) : |x - P_\phi| = \rho\},$$

where $x = (r\cos\theta, r\sin\theta)$. Let $A_\alpha(\rho, \phi)$ be the arc of the circle $C(\rho, \phi)$ with an angular span of α. This is given by

$$A_\alpha(\rho, \phi) = \{(r, \theta) \in [0, \infty) \times [0, 2\pi) : |x - P_\phi| = \rho,$$
$$\theta \in [\phi - \alpha, \phi + \alpha]\}.$$

We define the CAR transform of f over the arc $A_\alpha(\rho, \phi)$ as follows:

$$g^\alpha(\rho, \phi) = \mathcal{R}_\alpha f(\rho, \phi) = \int_{A_\alpha(\rho, \phi)} f(r, \theta) \, \mathrm{d}s, \qquad (1)$$

where $\mathrm{d}s$ is the arc length measure on the circle $C(\rho, \phi)$ and $A_\alpha(\rho, \phi)$ is the arc over which the integral is computed (see Fig. 2) with $\rho \in (0, R - \epsilon)$, $\epsilon > 0$.

Since both $f(r, \theta)$ and $g^\alpha(\rho, \phi)$ are 2π periodic in the angular variable, we may expand them into their respective Fourier series as follows.:

$$f(r, \theta) = \sum_{n=-\infty}^{\infty} f_n(r) \, e^{\mathrm{i}n\theta} \qquad (2)$$

$$g^\alpha(\rho, \phi) = \sum_{n=-\infty}^{\infty} g_n^\alpha(\rho) \, e^{\mathrm{i}n\phi}, \qquad (3)$$

where the coefficients $f_n(r)$, $g_n^\alpha(\rho)$ are given as follows:

$$f_n(r) = \frac{1}{2\pi} \int_0^{2\pi} f(r, \theta) \, e^{-\mathrm{i}n\theta} \mathrm{d}\theta$$

$$g_n^\alpha(\rho) = \frac{1}{2\pi} \int_0^{2\pi} g^\alpha(\rho, \phi) \, e^{-\mathrm{i}n\phi} \mathrm{d}\phi.$$

Based on our assumption on the f, the Fourier series of f and g^α will converge almost everywhere [13]. We now use an approach similar to one followed by [11] for circular Radon transform, which is based on the classical work by Cormack [27] for the linear Radon case.

Using the Fourier series expansion of function $f(r,\theta)$ in Equation (1) we have

$$g^\alpha(\rho,\phi) = \sum_{n=-\infty}^{\infty} \int_{A_\alpha(\rho,\phi)} f_n(r)e^{\mathrm{in}\theta}\mathrm{d}\theta.$$

Since the arc $A_\alpha(\phi,\rho)$ is symmetrical about ϕ we may rewrite the integral as follows.

$$g^\alpha(\rho,\phi) = \sum_{n=-\infty}^{+\infty} \int_{A_\alpha^+(\rho,\phi)} f_n(r)\left(e^{\mathrm{in}\theta} + e^{\mathrm{in}(2\phi-\theta)}\right)\mathrm{d}s$$

where $A_\alpha^+(\rho,\phi)$ is the part of arc corresponding to $\theta \geq \phi$. Further we observe that

$$e^{\mathrm{in}\theta} + e^{\mathrm{in}(2\phi-\theta)} = 2e^{\mathrm{in}\phi}\cos n(\theta-\phi).$$

We therefore have

$$g^\alpha(\rho,\phi) = \sum_{n=-\infty}^{\infty} \int_{A_\alpha^+(\rho,\phi)} f_n(r)\cos[n(\theta-\phi)]e^{\mathrm{in}\phi}\mathrm{d}s.$$

Comparing with Equation (3) we have

$$g_n^\alpha(\rho) = \int_{A_\alpha^+(\rho,\phi)} f_n(r)\cos[n(\theta-\phi)]\mathrm{d}s. \quad (4)$$

From Fig. 2, a straightforward calculation gives

$$\theta - \phi = \arccos\left(\frac{r^2 + R^2 - \rho^2}{2rR}\right) \quad (5)$$

and

$$\mathrm{d}s = \frac{r\mathrm{d}r}{R\sqrt{1 - \left(\frac{\rho^2+R^2-r^2}{2\rho R}\right)^2}}. \quad (6)$$

Using Equations (5) and (6) in (4) we get

$$g_n^\alpha(\rho) = \int_{R-\rho}^{\sqrt{R^2+\rho^2-2R\rho\cos\alpha}}$$

$$\times \frac{r\cos\left(n\cos^{-1}\left(\frac{r^2+R^2-\rho^2}{2rR}\right)\right)f_n(r)}{R\sqrt{1 - \left(\frac{\rho^2+R^2-r^2}{2\rho R}\right)^2}}\mathrm{d}r \quad (7)$$

Letting $\cos(n\arccos x) = T_n(x)$ and $u = R - r$, we have

$$g_n^\alpha(\rho) = \int_{R-\sqrt{R^2+\rho^2-2\rho R\cos\alpha}}^{\rho} \frac{K_n(\rho,u)}{\sqrt{\rho-u}} F_n(u)\mathrm{d}u \quad (8)$$

where

$$F_n(u) = f_n(R-u)$$

and

$$K_n(\rho,u) = \frac{2\rho(R-u)T_n\left[\frac{(R-u)^2+R^2-\rho^2}{2R(R-u)}\right]}{\sqrt{(u+\rho)(2R+\rho-u)(2R-\rho-u)}}. \quad (9)$$
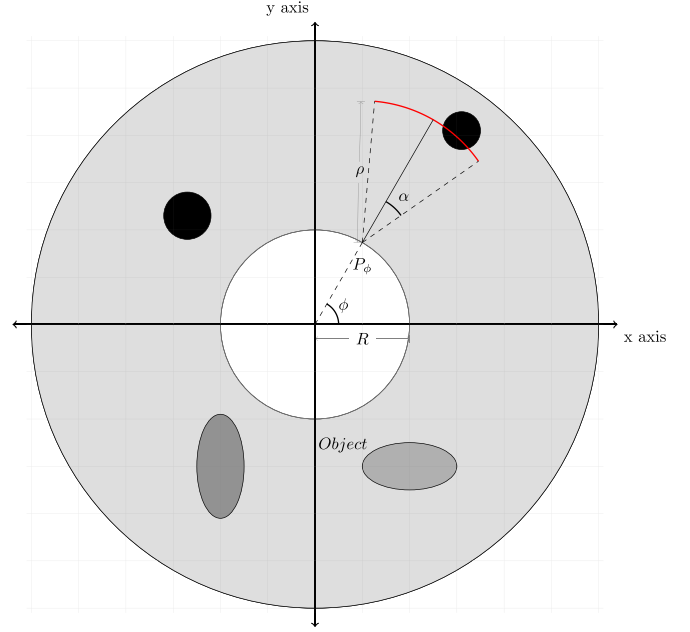

Fig. 3.   Setup for functions supported outside the acquisition circle.

B. Function Supported Outside Acquisition Circle

Next we consider the reconstruction of functions supported outside the acquisition circle. More precisely, we consider functions supported inside the annular region $A(R_1, R_2)$ where $R_1 = R$ is the inner radius and $R_2 = 3R$ is the outer radius of the annulus. R is the radius of the acquisition circle P. The acquisition setup for this case is illustrated in Fig. 3.

A similar derivation as above leads to the following Volterra integral equation of the first kind:

$$g_n^\alpha(\rho) = \int_{\sqrt{R^2+\rho^2+2\rho R\cos\alpha}}^{R+\rho} \frac{rT_n\left(\frac{R^2+r^2-\rho^2}{2rR}\right)}{\sqrt{1 - \left(\frac{R^2+\rho^2-r^2}{2\rho R}\right)^2}} f_n(r)\,\mathrm{d}r. \quad (10)$$

Substituting $u = r - R$ we have

$$g_n^\alpha(\rho) = \int_{\sqrt{R^2+\rho^2+2\rho R\cos\alpha}\,-R}^{\rho} \frac{F_n(u)\cdot K_n(\rho,u)}{\sqrt{\rho-u}}du \quad (11)$$

where $F_n(u) = f(R+u)$ and

$$K_n(\rho,u) = \frac{2\rho(R-u)\cdot T_n\left(\frac{(R-u)^2+R^2-\rho^2}{2R(R-u)}\right)}{\sqrt{(u+\rho)(2R+\rho-u)(2R-\rho-u)}}.$$

Note that in this case, the kernel of the integral transform is the same as in Equation (8), but, as is to be expected, the limits of the integral are different.

The analogue of Equations (8) and (11) arising in full circular Radon transform are Volterra integral equations of first kind, where one of the limits is fixed. These were studied in [11], [12]. An exact solution of such equations arising in full circular Radon transform is known. However, the exact solution is numerically unstable. An efficient numerical algorithm for the inversion of Volterra integral equations of the first kind appearing in [11],

[12] recently appeared in [21]. In the case under consideration, however, both the limits of integration are variable, and we are unable to address the question of existence and uniqueness of solutions to such integral equations in this work. Instead, we discretize the integral equation following the algorithm given in [21]. For this discrete problem, a unique solution exists, and we present an efficient numerical inversion method to deal with the inversion of such nonstandard Volterra integral equations of the first kind. The presence of edges of the circular arcs in the domain introduces artifacts in the reconstructed images. Furthermore, the fixed angular span α places restrictions on the edges that are visible, leading to a streak-like artifacts. We propose an artifact suppression strategy that reduces some of these artifacts in this paper. To invert the transform, we directly discretize Equation (8) and invert using a Truncated Singular value Decomposition (TSVD); a method originally proposed in [28]. In the next section, we explain the numerical inversion algorithm as well as a method for the suppression of artifacts.

III. NUMERICAL INVERSION

A. Forward Transform

The forward transform is computed by discretizing Equation (1). It may be noted that we consider data till half of the dimater only. The discrete transform is computed for $\rho \in [0, R - \epsilon_\rho]$, $\epsilon_\rho > 0$. We have

$$g^\alpha(\rho_k, \phi_p) = \sum_{(x_n, y_m) \in \mathcal{A}_{k,p}} f(x_n, y_m), \qquad (12)$$

where

$$\mathcal{A}_{k,p} = \left\{ (x_n, y_m) : \sqrt{(x_n - R\cos\phi_p)^2 + (y_m - R\sin\phi_p)^2} \right.$$

$$\left. = \rho_k^2, \phi_p - \alpha \leq \arctan\left(\frac{y_m}{x_n}\right) \leq \phi_p + \alpha \right\},$$

$$\rho_k = kh, k = 0, 1, \ldots, M - 1, \quad h = \frac{R - \epsilon_\rho}{M},$$

and

$$\phi_p = pl, j = 0, 1, \ldots, N - 1, \quad l = \frac{2\pi}{N}.$$

Note that $g^\alpha(\rho_k, \phi_p)$ is an $M \times N$ matrix. Fig. 4 shows an image $f(x, y)$ and the corresponding CAR transform g^α for $\alpha = 25°$ and $M = N = 300$.

B. Computation of Fourier Series

Given the data matrix $g^\alpha(\rho_k, \phi_p)$, we compute the discrete Fourier series coefficients g_n^α using the FFT algorithm. We as-
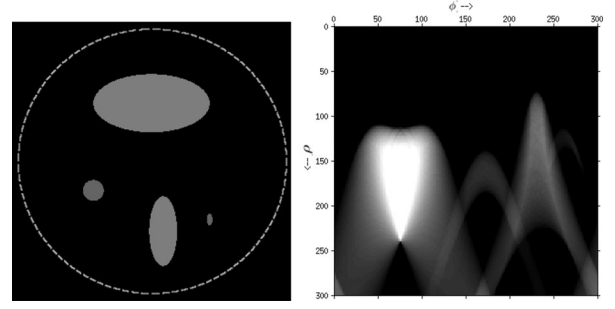

Fig. 4. Sample image and corresponding Circular arc Radon transform for $\alpha = 25°$. The dotted circle surrounding the image represents the acquisition circle.

sume the matrix $g^\alpha(\rho_k, \phi_p)$ to be real. Note that g_n^α is a vector of length M given by

$$g_n^\alpha(\rho_k) = \sum_{p=0}^{N-1} g^\alpha(\rho_k, \phi_p) \cdot e^{-i2\pi n \frac{p}{N}}.$$

C. Computation of Forward Transformation Matrix

Equation (8) can be discretized and written in the matrix form as follows

$$g_n^\alpha = B_n F_n \qquad (13)$$

where

$$g_n^\alpha = \begin{pmatrix} g_n^\alpha(\rho_0) \\ \cdot \\ \cdot \\ \cdot \\ g_n^\alpha(\rho_{M-1}) \end{pmatrix} \quad F_n = \begin{pmatrix} F_n(\rho_0) \\ \cdot \\ \cdot \\ \cdot \\ F_n(\rho_{M-1}) \end{pmatrix}$$

Matrix B_n is a piecewise linear, discrete approximation of the integral kernel in Equation (8), g_n^α is the Fourier series coefficients of the circular arc Radon data and F_n the Fourier series coefficients of the original unknown function. The matrix B_n is computed using the trapezoidal rule [22], [23]. The method essentially breaks the full integral into a sum of M integrals. The function is approximated to be linear in each interval so that

$$\sqrt{h} \left\{ \sum_{q=l}^{k} b_{kq} K_n(\rho_k, \rho_q) F_n(\rho_q) \right\} = g_n(\rho_k) \qquad (14)$$

where unnumbered eqn. shown at the bottom of the page, and $l = \max(0, \lfloor R - \sqrt{R^2 + \rho_k^2 - 2\rho_k R\cos\alpha} \rfloor)$ where $\lfloor x \rfloor$ is the greatest integer less than equal to x.

The detailed derivation of Equation (14) is given in Appendix A. From Equation (14) it is clear that the entries

$$b_{kq} = \begin{cases} \frac{4}{3}\{(k-q+1)^{\frac{3}{2}} + \frac{4}{3}(k-q)^{\frac{3}{2}} + 2(k-q)^{\frac{1}{2}} & q = l \\[2mm] \frac{4}{3}\left((k-q+1)^{\frac{3}{2}} - 2(k-q)^{\frac{3}{2}} + (k-q-1)^{\frac{3}{2}}\right) & q = l+1, \ldots k-1. \\[2mm] \frac{4}{3} & q = k. \end{cases}$$

of matrix B_n are independent of both the data $g^\alpha(\rho_k, \phi_p)$ as well as the function f to be recovered. Hence, the matrix B_n may be pre-computed and stored.

From Equation (14) we have

$$[B_n]_{kk} = \frac{4}{3}\sqrt{h} \neq 0 \quad \text{also,} \quad [B_n]_{kq} = 0 \; \forall \; q > k$$

$$\Rightarrow \det(B_n) = \left(\frac{4}{3}\sqrt{h}\right)^M \neq 0.$$

Therefore solution F_n of Equation (13) exists and is unique. However, the existence and uniqueness of solution in the continuous case (Equation 8) does not follow from the discrete case and a proof for the continuous case is an open question.

While the B_n matrix is invertible, in practice, it is ill-conditioned. In order to obtain a numerically stable inverse, we use Truncated Singular Value Decomposition (TSVD) based pseudo-inverse of the matrix. The TSVD based method is explained briefly in the next section.

D. Inversion using Truncated Singular Value Decomposition

TSVD is a commonly used technique to compute the pseudo-inverse of matrices. This method was introduced in [28] as a numerically stable method for solving least squares problem. The method involves the following steps.

1) Consider the singular value decomposition of matrix B_n such that $B_n = U D_n V^T$. D_n is an $n \times n$ diagonal matrix of singular values of B_n and U, V are orthogonal matrices consisting of left and right singular vectors of B_n respectively.

2) A rank r approximation $B_{n,r}$ of the matrix B_n, is given by $B_{n,r} = U D_r V^T$, where D_r is a diagonal matrix with

$$D_r(i,i) = \begin{cases} D_n(i,i) = \sigma_i, & i \leq r \\ 0 & i > r. \end{cases}$$

3) Then the rank r inverse of the matrix is given by $B_{n,r}^{-1} = V D_r^{-1} U^T$ where,

$$D_{i,i}^{-1} = \begin{cases} \dfrac{1}{\sigma_i} & i < r \\ 0 & \text{otherwise} \end{cases}$$

4) Using $B_{n,r}^{-1}$ in Equation 13 we have

$$F_n \approx B_{n,r}^{-1} g_n$$

5) The approximation of original function $f(r, \theta)$ may be obtained by computing inverse Fourier transform of F_n.

$$f(r_k, \theta_n) = \sum_{p=0}^{N-1} F_n(R - \rho_k, \phi_p) \cdot e^{i2\pi n \frac{p}{N}}. \quad (15)$$

The final image $f(x, y)$ in the Cartesian coordinates is obtained by interpolating the the polar image $f(r_k, \theta_n)$ onto the Cartesian grid using bilinear interpolation. Algorithm 1 summarizes the steps involved in the numerical inversion.

Algorithm 1: Numerical Inversion Algorithm.

Data: Radon Transform, $g^\alpha(\rho, \phi)$

Result: $f(r, \theta)$

1 Compute the Discrete Fourier series $g_n^\alpha(\rho)$, of input $g^\alpha(\rho, \phi)$ in the ϕ variable s.t.
$$g_n^\alpha(\rho_k) = \sum_{p=0}^{N-1} g^\alpha(\rho_k, \phi_p) \cdot e^{-i2\pi n \frac{p}{N}}$$

2 **for** each n **do**

3   Compute $B_n = [a_{ij} K_{ij}^n]$ where, a_{ij} is given by equation 14, and $K_{ij}^n = K_n(\rho_i, \rho_j)$ by equation 9

4   Let $B_{n,r} = U D_r V^T$, with $D_r = diag(\sigma_1, ... \sigma_r)$, s.t SVD of $B_n = U D_n V^T$,

5   Compute low rank inverse, $B_{n,r}^{-1} = V D_r^{-1} U^T$

6     $F_n = B_{n,r}^{-1} \; g_n^\alpha$

7 **end**

8 Compute inverse Fourier transform f using Equation (15).
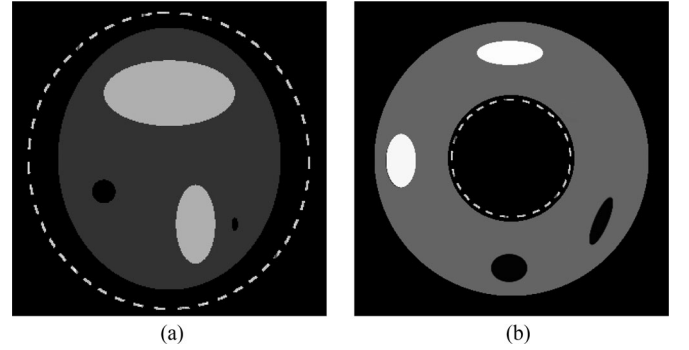

Fig. 5. Phantoms used in the experiments. The dotted circle represents the acquisition circle. (a) Phantom with support inside, (b) Phantom with support outside.

IV. EXPERIMENTS AND RESULTS

We use the strategy discussed in Section III to reconstruct analytical phantoms shown in Fig. 5. During reconstruction, the view angle α will be determined by the transducer, while the discretisation of angular and radial variables are chosen as part of an imaging protocol depending on constraints on acquisition time, sensor bandwidth and sensitivity.

At the algorithm level, a key parameter affecting the quality of reconstruction is the rank r of the matrix $B_{n,r}$. The matrix B_n is non-singular, however due to the high condition number $\left(\mathcal{O}(10^{15})\right)$, a full rank $(r = n)$ inversion will be unstable and will not result in a meaningful reconstruction. Therefore, an r-rank (with $r < n$,) approximation of the matrix B_n is one approach to stable inversion. Such a low-rank approximation is achieved in the proposed numerical scheme via TSVD.

The SVD decomposes a signal f into a sum of harmonics $f = \sum_{i=1}^{n} \sigma_i u_i v_i^T$. Consequently, setting $\sigma_i = 0$ for $i > r$ in the TSVD of $B_{n,r}$ will lower the number of harmonics in the reconstructed image leading to ringing artifacts. Fig. 6 shows reconstruction for a fixed view angle $\alpha = 31°$ with different r. The results are as expected, with good quality reconstruction
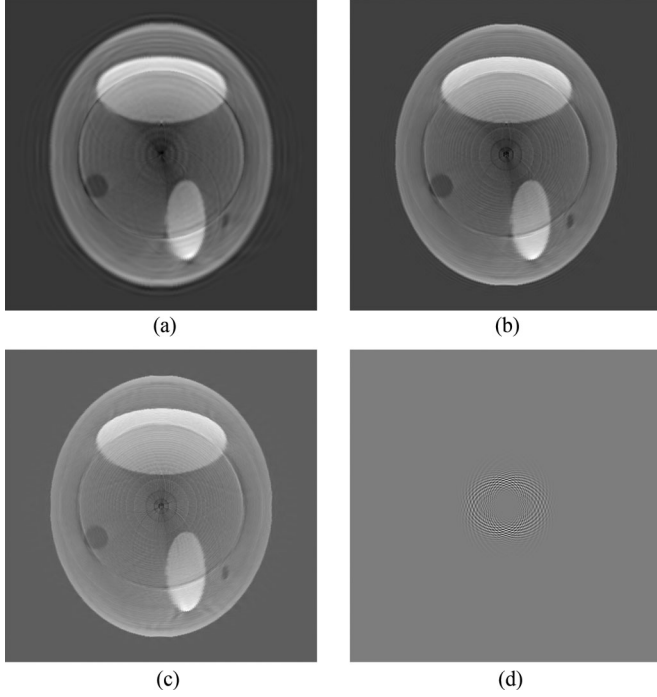
Fig. 6. Effect of rank r of matrix $B_{n,r}$ on the reconstruction quality. n = 300 in all the above examples. (a) Rank = $n/6$, (b) Rank = $n/2$, (c) Rank = $9n/10$, (d) Rank = n.
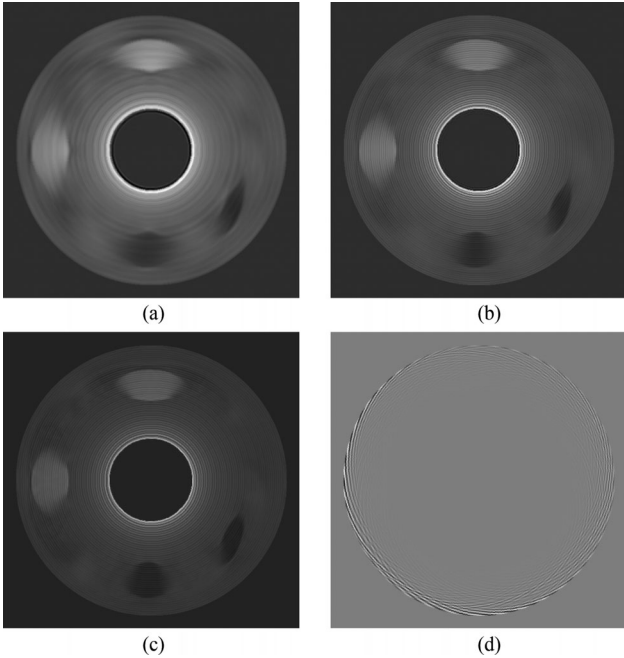

Fig. 7. Effect of rank r of matrix $B_{n,r}$ for support outside case. n = 300 in all examples. (a) Rank = $n/6$, (b) Rank = $n/2$, (c) Rank = $9n/10$, (d) Rank = n.

seen for $r = 0.9n$ and visible degradation in the quality with a reduction in r. Specifically, severe ringing artifacts can be seen in the result when $r = 0.5n$ or lower. Thus, there is a tradeoff between rank and quality of reconstruction. Fig. 7 shows a similar relation for the case of object supported outside the acquisition circle.

Despite the fact that the view angle is a parameter that is generally fixed for a particular imaging setup, it is of interest to gain insight into the relationship between this parameter and the quality of reconstruction. In general, limiting the view by restricting the angular span α should introduce artifacts, as all edges in the object may not be visible. This notion of visibility can be explained as follows. If the data set $\mathcal{C}$ representing the curves of integration, are smooth objects such as lines, full circles, spheres etc., then roughly speaking, for an edge in the image to be stably reconstructed, there should be an element of $\mathcal{C}$ tangential to the edge. A formal justification of this statement is possible with the tools of Fourier integral operator theory and microlocal analysis [25], [29], [30]. We refer to all edges which are tangential to the interiors of the arcs in the data set $\mathcal{C}$, as visible edges. Edges which fail to satisfy this condition are not reconstructed stably. Such a principle, for our set up, can be applied for edges at points where the interiors of the arcs satisfy the aforementioned tangential condition. However, due to the corners of the arcs inside the domain, we expect artifacts to be present in the reconstructed image. A rigorous study of the microlocal analysis of CAR transform, in particular, the characterization of the added artifacts into the reconstructed image is an important and challenging problem and we hope to address this in a future work. Fig. 10 shows reconstruction at $r = 0.9n$ for various α. We observe from these results that, as expected, the reconstruction of the visible edges is sharp, whereas the other edges are blurred out. As the angle α increases, the visible region of edges increases, and hence most of the edges in the images with large α are reconstructed. Larger α corresponds to a wider arc, and therefore more edges are tangential to the curve of integration. This dependence on α is clearly observed in the lower ellipse in Fig. 10. As the span of arc increases, some arcs become tangential to the lower boundary of the ellipse. Hence we observe that the lower portion of the ellipse becomes sharper as α increases. A similar behavior is also observed in Fig. 11 where the support of the function is outside the acquisition circle. In this Figure, there are circular arcs in the data set tangential to the edges in a neighborhood of the radial direction whereas none is tangential in the complement of such directions. Therefore, these edges are blurred out and the reconstruction of the edges does not appear to improve with increasing α.

We also observe various streaks and a strong circular artifact whose location changes with α. These artifacts are to be expected as we are dealing with a limited view problem. Handling of these artifacts to improve the quality of reconstructed image is considered in the next section.

V. SUPPRESSION OF ARTIFACTS

To understand the source of artifacts, and subsequent suppression in the reconstructed images we re-write the CAR transform (equation 1) as follows.

$$g^\alpha(\rho, \phi) = \mathcal{R}_\alpha f(\rho, \phi) = \int_{C(\rho,\phi)} \chi_A f(r, \theta) \, ds, \qquad (16)$$
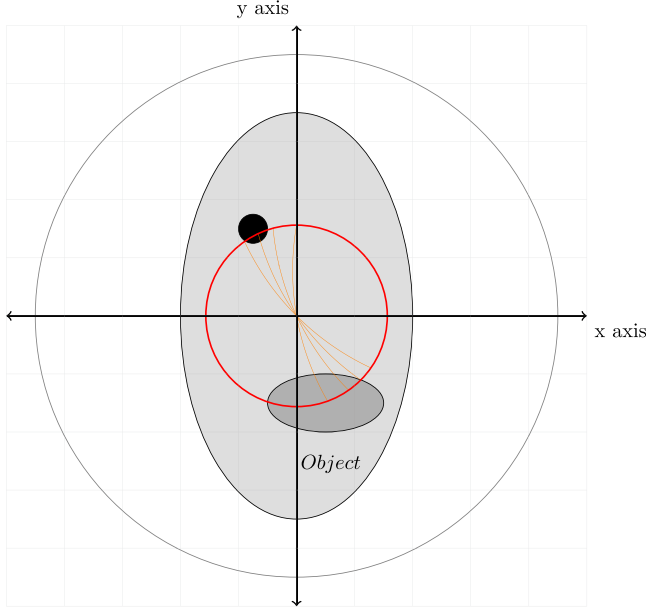
Fig. 8.   Location of sharp artifact(red circle) with respect to the arcs(orange).

Algorithm 2: Numerical Inversion Algorithm.

Data: Radon Transform, $g^\alpha(\rho, \phi)$

Result: $f(r, \theta)$

1 Compute the Discrete Fourier series $g_n^\alpha(\rho)$, of input $g^\alpha(\rho, \phi)$ in the ϕ variable s.t.

$$g_n^\alpha(\rho_k) = \sum_{p=0}^{N-1} g^\alpha(\rho_k, \phi_p) \cdot e^{-i2\pi n \frac{p}{N}}$$

2 **for** *each n* **do**

3 | Compute $B_n = [\hat{b}_{ij} K_{ij}^n]$ where $\hat{b}_{ij}$ is given by

4 |

$$\hat{b}_{ij} = \begin{cases} e^{\frac{-(j-m)^2}{\sigma^2}} b_{ij}, & j < m \\ b_{ij}, & m \le j \le i \end{cases}$$

| where b_{ij} is given by equation 14 with $l = 0$, $m = max\left(0, \left\lfloor R - \sqrt{R^2 + \rho_k^2 - 2\rho_k R \cos\alpha} \right\rfloor\right)$ and $K_{ij}^n = K_n(\rho_i, \rho_j)$ given by equation 9

5 | Let $B_{n,r} = U D_r V^T$, with $D_r = diag(\sigma_1, ... \sigma_r)$, s.t SVD of $B_n = U D_n V^T$,

6 | Compute low rank inverse, $B_{n,r}^{-1} = V D_r^{-1} U^T$

7 | $F_n = B_{n,r}^{-1} \; g_n^\alpha$

8 **end**

9 Compute inverse Fourier transform f using equation (15).

Fig. 9.   Structure of matrix B_n. The original matrix (left) has a sharp cut off in the entries of B_n, while in the modified matrix (right) they decay smoothly. (a) original matrix Structure, (b) Modified matrix Structure.

---

where, χ_A is the characteristic function of the arc $A_\alpha(\rho, \phi)$ such that

$$\chi_A = \begin{cases} 1, & (r, \theta) \in A_\alpha(\rho, \phi) \\ 0, & \text{else} \end{cases}$$

The function χ_A truncates the full data $f(r, \theta)$ before computation of the integral. χ_A is a Heaviside type function with sharp cut-off at the edges of the arc. Since the data is measured only for $\rho \in (0, R - \epsilon_\rho)$, there is also a similar Heaviside type truncation function in the radial direction, with hard truncation at $\rho = R - \epsilon_\rho$.

It should be noted that $\chi_A \equiv 1$ for the whole circle $C(\rho, \phi)$ in the circular Radon transform while, $\chi_A = 0$ beyond the arc $A_\alpha(\rho, \phi)$ in the CAR transform. The sharp truncation in data should lead to strong streaking artifacts in the reconstructed result. Moreover, a strong circular artifact is also observed along the edges of arcs corresponding to largest value of ρ as depicted in Fig. 8. The double penalization in the form of hard truncation of data i) at the edges of the arc in the angular direction and ii) in the radial direction for $\rho = R - \epsilon_\rho$, we believe, is the reason for the sharp circular artifact at a specific radial location.

In order to suppress the artifacts, we modify the characteristic function to $\hat{\chi}_A$, so that it decays smoothly instead of going to 0 abruptly at the edge. This smooth decay serves to remove the singularity due to the Heaviside-type truncation. We choose a smooth, squared exponential decay of the form $e^{\frac{-x^2}{\sigma^2}}$. Specifically, the values of the matrix B_n are weighted by an exponential decay factor of the form $e^{\frac{-(j-m)^2}{\sigma^2}}$ as explained in Algorithm 2.

Here, σ controls the degree of smoothing. A large σ results in excessive smoothing and hence lead to blurring of the true edges of the reconstructed image. A low σ results in mimimal

smoothing, preserves edge definition but also in retention of artifacts. In our experiments, we chose $\sigma = 40$ which suppresses the strong streak artifacts, (see Fig. 10), whilst retaining the definition of true edges in the image. Algorithm 2 is a modified version of the numerical inversion Algorithm 1 and includes artifact suppression with $\hat{\chi}_A$.

As noted in Section III, matrix B_n is a lower triangular matrix. Fig. 9 is a visualization (as an image) of the structure of matrix B_n in the original and the modified form. Here, the white/black pixels indicate non-zero/zero entries. The modification of the transformation matrix leads to a slow decay of numerical values as shown in Fig. 9 with grey coloured pixels. This helps smooth the sharp circular artifacts generated in the inversion process. Note that only the matrix B_n, which is constant for a given setup, is changed in the modified algorithm. The data, $g^\alpha(\rho, \phi)$ is not changed or pre-processed in any form. Fig. 10, 11 show the reconstructed images after artifact suppression is performed for the cases of function supported inside and outside, respectively. We observe that using the modified algorithm, the sharp circular artifacts are significantly suppressed while the true edges of the image are retained.
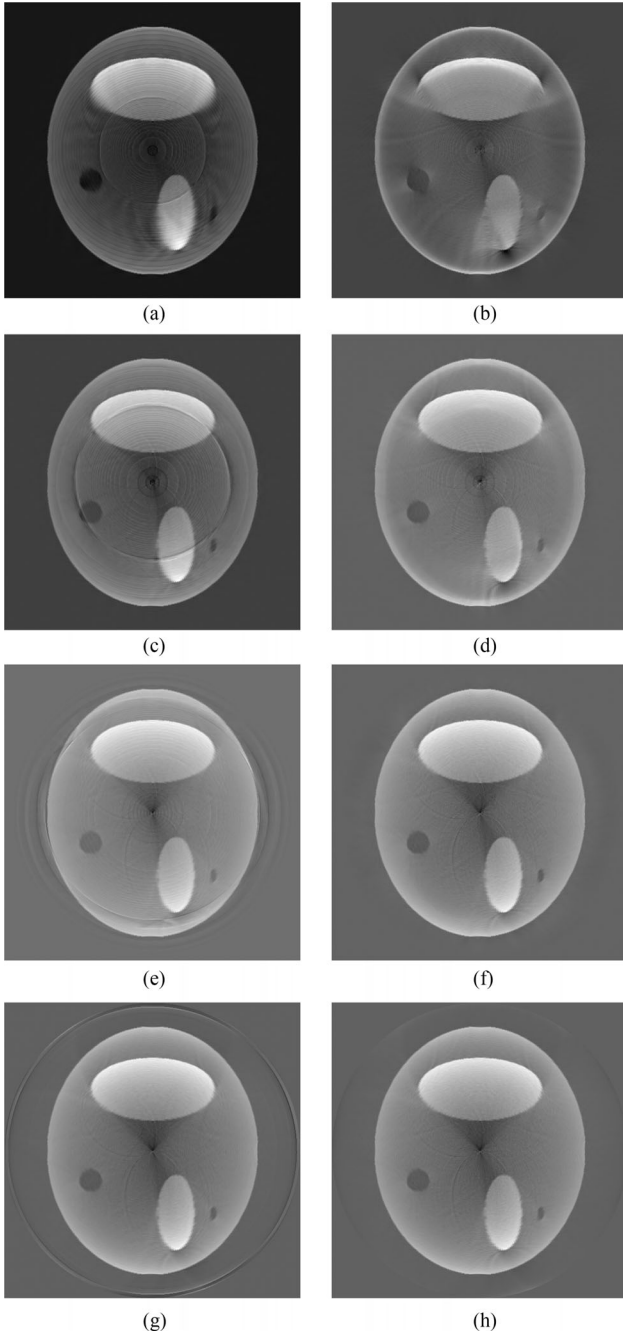
Fig. 10. Reconstructed images corresponding to different α before (column 1), and after artifact suppression (column 2), for the support inside case. (a) $\alpha = 21$, (b) $\alpha = 21$, (c) $\alpha = 31$, (d) $\alpha = 31$, (e) $\alpha = 46$, (f) $\alpha = 46$, (g) $\alpha = 76$, (h) $\alpha = 76$.
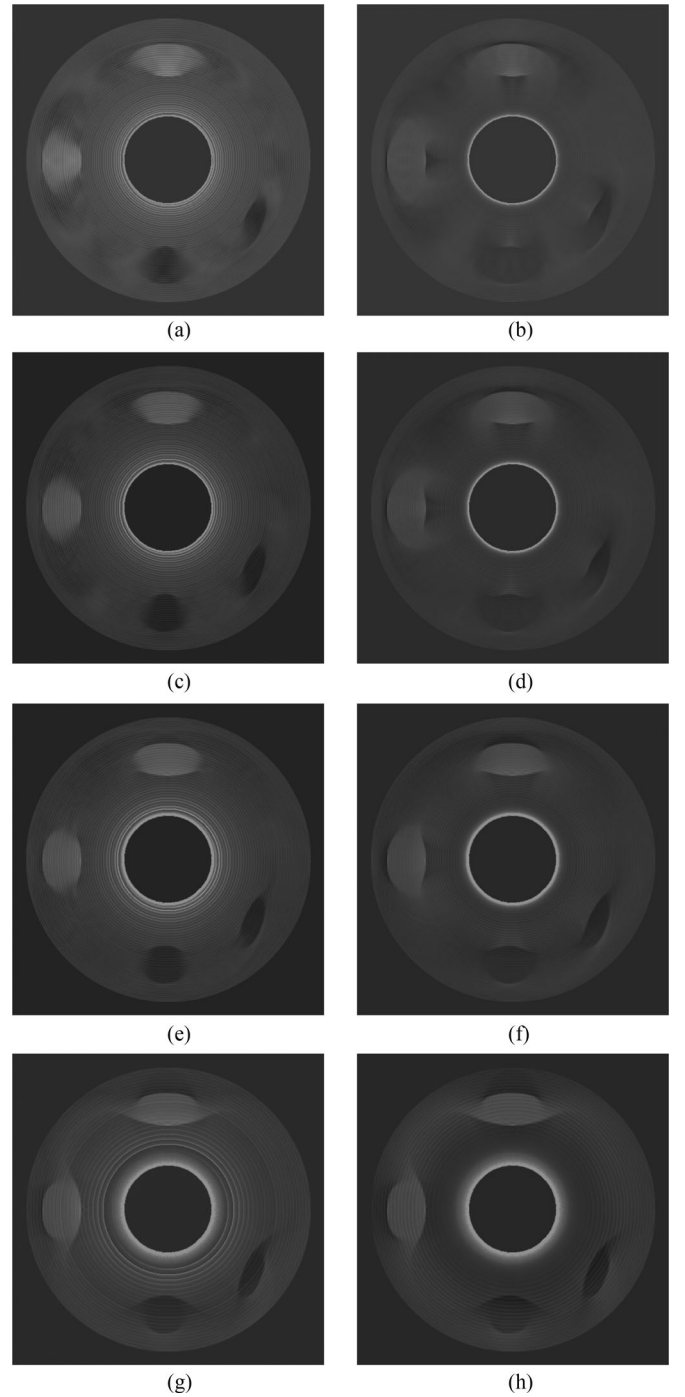

Fig. 11. Reconstructed images corresponding to different α before (column 1), and after artifact suppression (column 2), for the support outside case. (a) $\alpha = 21$, (b) $\alpha = 21$, (c) $\alpha = 31$, (d) $\alpha = 31$, (e) $\alpha = 46$, (f) $\alpha = 46$, (g) $\alpha = 76$, (h) $\alpha = 76$.

VI. CONCLUSION

We presented a numerical algorithm to invert CAR transform arising in some imaging applications. The numerical algorithm required the solution of ill-conditioned matrix problems which was accomplished using a TSVD method. The entries of the matrix are independent of the image function, and therefore the TSVD need to be done only once and can be used repeatedly for image reconstruction leading to an efficient image reconstruction algorithm.

Compared to the inversion of full circular Radon transform, the quality of image reconstruction in the case of CAR transform is poorer due to the following reasons. (a) The edges of the arcs of circles introduce strong artifacts. (b) Several edges of the image are invisible due to the limit in the angular span of the arcs. These lead to some "streak" and circular artifacts. We also presented a numerical algorithm for handling this problem and demonstrated it helps reduce some of these artifacts.

$$b_{kq} = \begin{cases} \frac{4}{3}\{(k-q+1)^{\frac{3}{2}} + \frac{4}{3}(k-q)^{\frac{3}{2}} + 2(k-q)^{\frac{1}{2}} & q = l \\ \frac{4}{3}\left((k-q+1)^{\frac{3}{2}} - 2(k-q)^{\frac{3}{2}} + (k-q-1)^{\frac{3}{2}}\right) & q = l+1,\dots k-1. \\ \frac{4}{3} & q = k. \end{cases}$$

The theoretical inversion of CAR leads to some very interesting non-standard Volterra integral equations of the first kind with weakly singular kernel, that to the best of our knowledge, have not been dealt with in current literature. We hope to address them in our future work.

ACKNOWLEDGMENT

The authors would like to thank Gaik Ambartsoumian, Souvik Roy, and Todd Quinto for several fruitful discussions.

APPENDIX A
TRAPEZOIDAL INTEGRATION

The Fourier coefficients of the forward transform are given by equation 8 restated below.

$$g_n^\alpha(\rho) = \int_{R-\sqrt{R^2+\rho^2-2\rho R\cos\alpha}}^{\rho} \frac{F_n(u)K_n(\rho,u)}{\sqrt{\rho-u}}dr.$$

The integral is approximated by the sum in Equation (14). The sum is obtained by the trapezoidal product integration method proposed in [22], [23] (see also [21]) which we briefly outline below. Let M be a positive integer and $\rho_l = lh$, $l = 0,\dots,M$ and $h = \frac{R-\epsilon}{M}$ be a discretization of radial variable $\rho \in [0, R-\epsilon]$ The above equation may be rewriten as follows

$$g_n^\alpha(\rho_k) = \sum_{q=1}^{k} \int_{\rho_{q-1}}^{\rho_q} \frac{F_n(u)K_n(\rho,u)}{\sqrt{\rho-u}}du.$$

We approximate $F_n(u) \cdot K_n(\rho,u)$ by linear function in the interval $[\rho_{q-1}, \rho_q]$, such that

$$F_n(u)K_n(\rho,u) \approx F_n(\rho_{q-1})K_n(\rho_k,\rho_{q-1})\frac{\rho_q - u}{h}$$
$$+ F_n(\rho_q)K_n(\rho_k,\rho_q)\frac{u-\rho_{q-1}}{h}.$$

Here the function takes values $F_n(\rho_{q-1})K_n(\rho_k,\rho_{q-1})$ and $F_n(\rho_q)K_n(\rho_k,\rho_q)$ at the end points of the interval respectively. Hence we have

$$g_n^\alpha(\rho_k) = \sum_{q=1}^{k} \int_{\rho_{q-1}}^{\rho_q} \frac{1}{\sqrt{\rho-u}}\left[F_n(\rho_{q-1})K_n(\rho_k,\rho_{q-1})\frac{\rho_q - u}{h}\right.$$
$$\left. + F_n(\rho_q)K_n(\rho_k,\rho_q)\frac{u-\rho_{q-1}}{h}\right]du.$$

Simple integration gives

$$h^{\frac{-3}{2}}\int_{\rho_{q-1}}^{\rho_q} \frac{\rho_q - u}{\sqrt{\rho_k - u}}du = -\frac{4}{3}\{(k-q+1)^{\frac{3}{2}} - (k-q)^{\frac{3}{2}}\}$$
$$+ 2(k-q+1)^{\frac{1}{2}}$$

and,

$$h^{\frac{-3}{2}}\int_{\rho_{q-1}}^{\rho_q} \frac{u - \rho_{q-1}}{\sqrt{\rho_k - u}}du = \frac{4}{3}\{(k-q+1)^{\frac{3}{2}} - (k-q)^{\frac{3}{2}}\}$$
$$- 2(k-q)^{\frac{1}{2}}.$$

Hence we have

$$g_n^\alpha(\rho_k) = \sqrt{h}\sum_{q=l}^{k}\left[-\frac{4}{3}\{(k-q+1)^{\frac{3}{2}} - (k-q)^{\frac{3}{2}}\} + 2(k-q+1)^{\frac{1}{2}}\right]$$
$$\times F_n(\rho_{q-1})K_n(\rho_k,\rho_{q-1})$$
$$+ \left[\frac{4}{3}\{(k-q+1)^{\frac{3}{2}} - (k-q)^{\frac{3}{2}}\} - 2(k-q)^{\frac{1}{2}}\right]$$
$$\times F_n(\rho_q)K_n(\rho_k,\rho_q).$$

From the support assumption, we have $F_n(p) = 0 \ \forall p \le 0$. Then the above expression simplifies to the following expression.

$$\sqrt{h}\left\{\sum_{q=l}^{k} b_{kq}K_n(\rho_k,\rho_q)F_n(\rho_q)\right\} = g_n(\rho_k)$$

where unnumbered eqn. shown at the top of the page, and $l = \max\left(0, \lfloor R - \sqrt{R^2 + \rho_k^2 - 2\rho_k R\cos\alpha}\rfloor\right)$ where $\lfloor x \rfloor$ is the greatest integer less than equal to x.

REFERENCES

[1] X. Wang, X. Xie, G. Ku, L. V. Wang, and G. Stoica, "Noninvasive imaging of hemoglobin concentration and oxygenation in the rat brain using high-resolution photoacoustic tomography," *J. Biomed. Opt.*, vol. 11, no. 2, 2006, Art. no. 024 015.

[2] M.-L. Li *et al.*, "Simultaneous molecular and hypoxia imaging of brain tumors in vivo using spectroscopic photoacoustic tomography," *Proc. IEEE*, vol. 96, no. 3, pp. 481–489, Mar. 2008.

[3] X. Wang, Y. Pang, G. Ku, X. Xie, G. Stoica, and L. V. Wang, "Noninvasive laser-induced photoacoustic tomography for structural and functional in vivo imaging of the brain," *Nature Biotechnol.*, vol. 21, no. 7, pp. 803–806, 2003.

[4] Y. Lao, D. Xing, S. Yang, and L. Xiang, "Noninvasive photoacoustic imaging of the developing vasculature during early tumor growth," *Phys. Med. Biol.*, vol. 53, no. 15, pp. 4203–4212, 2008.

[5] G. Ku, X. Wang, X. Xie, G. Stoica, and L. V. Wang, "Imaging of tumor angiogenesis in rat brains in vivo by photoacoustic tomography," *Appl. Opt.*, vol. 44, no. 5, pp. 770–775, 2005.

[6] P. Kuchment and L. Kunyansky, "Mathematics of photoacoustic and ther-moacoustic tomography," in *Handbook of Mathematical Methods in Imaging*. New York, NY, USA: Springer, 2011, pp. 817–865.

[7] P. Burgholzer, J. Bauer-Marschallinger, H. Grün, M. Haltmeier, and G. Paltauf, "Temporal back-projection algorithms for photoacoustic tomography with integrating line detectors," *Inverse Probl.*, vol. 23, no. 6, p. S65, 2007.

[8] R. G. Kolkman, E. Hondebrink, W. Steenbergen, T. G. van Leeuwen, and F. F. de Mul, "Photoacoustic imaging of blood vessels with a double-ring sensor featuring a narrow angular aperture," *J. Biomed. Opt.*, vol. 9, no. 6, pp. 1327–1335, 2004.

[9] M. Xu and L. V. Wang, "Time-domain reconstruction for thermoacoustic tomography in a spherical geometry," *IEEE Trans. Med. Imaging*, vol. 21, no. 7, pp. 814–822, Jul. 2002.

[10] M. Xu, G. Ku, and L. V. Wang, "Microwave-induced thermoacoustic tomography using multi-sector scanning," *Med. Phys.*, vol. 28, no. 9, pp. 1958–1963, 2001.

[11] G. Ambartsoumian, R. Gouia-Zarrad, and M. A. Lewis, "Inversion of the circular Radon transform on an annulus," *Inverse Probl.*, vol. 26, no. 10, 2010, Art. no. 105015.

[12] G. Ambartsoumian and V. P. Krishnan, "Inversion of a class of circular and elliptical Radon transforms," *Amer. Math. Soc.*, vol. 653, pp. 1–12, 2015.

[13] Y. Katznelson, *An Introduction to Harmonic Analysis*, 3rd ed. Cambridge, U.K.: Cambridge Univ. Press, 2004, pp. xviii+314.

[14] V. P. Palamodov, "Reconstruction from limited data of arc means," *J. Fourier Anal. Appl.*, vol. 6, no. 1, pp. 25–42, 2000.

[15] T. T. Truong and M. K. Nguyen, "Radon transforms on generalized Cormack's curves and a new Compton scatter tomography modality," *Inverse Probl.*, vol. 27, no. 12, 2011, Art. no. 125 001.

[16] A. S. Apartsyn, *Nonclassical linear Volterra Equations of the First Kind, (ser. Inverse and Ill-posed Problems Series)*. Utrecht, the Netherlands: VSP, 2003.

[17] A. S. Apartsyn, "On some classes of linear Volterra integral equations," *Abstr. Appl. Anal.*, 2014, Art. no. 532409.

[18] D. N. Sidorov, "Solvability of systems of Volterra integral equations of the first kind with piecewise continuous kernels," *Russian Math.*, vol. 57, no. 1, pp. 54–63, 2013.

[19] D. N. Sidorov, "Generalized solution to the Volterra equations with piecewise continuous kernels," *Bull. Malaysian Math. Sci. Soc.*, vol. 37, no. 3, pp. 757–768, 2014.

[20] N. A. Sidorov and D. N. Sidorov, "On the solvability of a class of Volterra operator equations of the first kind with piecewise continuous kernels," *Math. Notes*, vol. 96, nos. 5–6, pp. 811–826, 2014.

[21] S. Roy, V. P. Krishnan, P. Chandrashekar, and A. S. V. Murthy, "An efficient numerical algorithm for the inversion of an integral transform arising in ultrasound imaging," *J. Math. Imaging Vis.*, vol. 53, no. 1, pp. 78–91, 2015.

[22] R. Weiss, "Product integration for the generalized Abel equation," *Math. Comp.*, vol. 26, pp. 177–190, 1972.

[23] R. Plato, "The regularizing properties of the composite trapezoidal method for weakly singular Volterra integral equations of the first kind," *Adv. Comput. Math.*, vol. 36, no. 2, pp. 331–351, 2012.

[24] G. Ambartsoumian and S. Roy, "Numerical inversion of a class of broken ray transforms arising in single scattering optical tomography," *IEEE Trans. Comput. Imaging*, vol. 2, no. 2, pp. 166–173, 2016.

[25] L. Hörmander, "Fourier integral operators, I," *Acta Math.*, vol. 127, pp. 79–183, 1971.

[26] F. Trèves, *Introduction to Pseudodifferential and Fourier Integral Operators, vol. 1*. New York, NY, USA: Plenum Press, 1980.

[27] A. M. Cormack, "Representation of a function by its line integrals, with some radiological applications," *J. Appl. Phys.*, vol. 34, no. 9, pp. 2722–2727, 1963.

[28] G. Golub and W. Kahan, "Calculating the singular values and pseudo-inverse of a matrix," *J. Soc. Ind. Appl. Math., Series B: Numer. Anal.*, vol. 2, no. 2, pp. 205–224, 1965.

[29] V. Guillemin and S. Sternberg, *Geometric Asymptotics*. Providence, RI, USA: American Mathematical Society, 1977.

[30] F. Trèves, *Introduction to Pseudodifferential and Fourier Integral Operators. vol. 2*. New York, NY, USA: Plenum Press, 1980.

Tabish A. Syed received the B.Tech. degree in electronics and communication engineering (Hons.) from the International Institute of Information Technology (IIIT), Hyderabad, India, in 2014 and the M.S. (by research) degree in electronics and communication engineering from the Center for Visual Information Technology, IIIT, in 2016. He is currently working toward the Ph.D. degree at the Center for Intelligent Machines, McGill university, Montreal, QC, Canada. His research interests include signal processing, computed tomography, and mathematical problems of imaging.

Venkateswaran P. Krishnan received the Ph.D. degree in mathematics from the University of Washington, Seattle, WA, USA, in 2007. He is currently at TIFR Centre for Applicable Mathematics, Bangalore, India. His research interests include inverse problems, partial differential equations, image reconstruction, and microlocal analysis.

Jayanthi Sivaswamy received the Ph.D. in electrical engineering from Syracuse University, Syracuse, NY, USA. Since 2001, she has been with International Institute of Information Technology, Hyderabad, India. Prior to that, she was with the University of Auckland, Auckland, New Zealand. Her research interests include the area of medical image analysis, CAD algorithm development in particular.